IX. Guidance and Control Analysis and Integration

GUIDANCE AND CONTROL DIVISION

A. Optimization and Reliability Calculations for Multi-Thermionic-Converter Systems,

R. Szejn and K. Shimada

1. Introduction

Power sources that make use of nuclear energy are one means of producing the electrical power necessary for deep space probes. Among such sources are thermionic energy converters, which have been shown to offer a large output power with a conversion efficiency as large as 15%. Although the converter technology has reached a point where it is feasible to implement these converters as a power source, the reliability of converters and systems using these devices has not been investigated well enough to arrive at a flyable system.

One method of developing a power supply having a high reliability is to use a large number of moderately reliable converters connected in a matrix configuration. An optimized configuration should be developed for each system, depending upon the system's power output, the component reliability, and the required system reliability.

In this article, approaches to optimization and reliability calculations are presented along with an analysis of one particular system. There are also some general qualitative remarks in regard to optimization and reliability as a function of system configuration, followed by a reliability analysis of a 150-W power system.

2. Approaches to Optimization and Reliability Calculations

Reliability has two meanings in the field of thermionics, depending on whether converter reliability or system reliability is being referred to. In the former case, a reliability of 0.95, for example, indicates that life tests on similarly designed units have shown 95 out of 100 to be still operating above some given performance level at the end of a life test. In the latter case, one speaks of having a certain system reliability at a specified output power. For example, one might have a system reliability of 0.8 for a relative power output of 0.9. This means that there is an 80% probability that the converter system will be delivering at least 90% of the original undegraded output power at the end of a mission. System reliability will be the topic of concern in this article.

There are three methods for determining a functional dependence between reliability and relative power. One method requires that the relative power output is calculated for every possible combination of failed diodes. This assumes two modes of failure—open or short—with some probability for an open failure P_o and some probability

for a shorted failure P_s. (Note that only abrupt failures are considered.)

This method gives the distinct power levels obtainable. Obviously, the number of failure combinations that need be calculated can be reduced if the symmetry involved is taken into account. For example, in a 2-series, 3-parallel cylindrical network, only one calculation is required to determine the power output one to one open failure, while there are six possible locations where the failure can occur. The reliability $R(W)$ at any one possible relative power output, $W(\leq 1.0)$, is given by

$$R(W) = 1 - \sum [\text{all probabilities that yield power degradation larger than } (1 - W)] \text{ (Ref. 1)}$$

This method is practical only for a very small system, since the number of distinct cases that must be treated grows quite rapidly with the number of diodes being used.

The second available method for determining reliability employs a Monte Carlo sampling scheme. The approach is to generate a random number between zero and one using a uniform pseudo-random number generator, and then, depending on the assigned converter reliability P, label the diode as good or bad according to whether the corresponding random number is less than or greater than P. If the diode is bad, then a second random number is generated to determine whether the failure is to be called an open or short. This simulated converter system is then analyzed to give a relative power value. This process is repeated a large number of times, resulting in a distribution curve from which the reliability curve can be deduced.

The final method also uses a sampling scheme, but in a more restricted sense (Ref. 2). Here the number of failures is specified and the random number generator merely picks the locations to be labeled as failures and at the same time dictates whether they are to be open or shorted failures. In this way, a distribution of relative power values is obtained for a given number of failures. The reliability curve is then determined by plotting the average relative power for r failures against the probability $P(r)$ of having r or less failures:

$$P(r) = \sum_{i=0}^{r} {}_nC_i \, P^{n-i} (1 - P)^i$$

where n is the number of converters in the system and ${}_nC_i = n!/i!\,(n - i)!$ These are the present methods being used in reliability studies; the next area of concern is optimization.

There are a number of factors to be considered in optimizing a system, but the one which is of interest here is the value of the interconnection resistance in a matrix of converters (Fig. 1). The optimized resistance is a function of the diode configuration and the probabilities of having open and shorted failures. The user will specify whether the system reliability is to be maximized at a particular power level, perhaps the minimum power level usable; or whether the reliability should be maximized at the upper power levels.

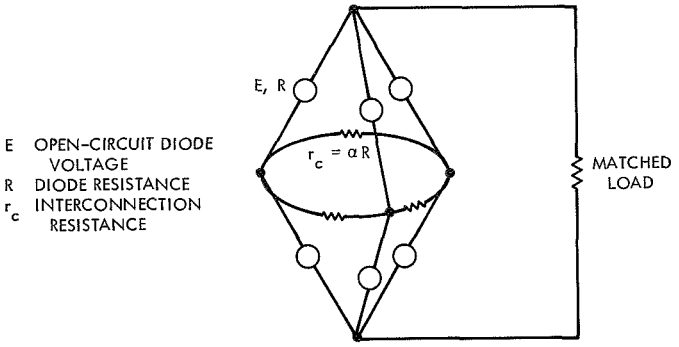

Fig. 1. Converter system configuration

The method for optimizing a converter system uses an iteration technique employing one of the methods mentioned above for determining the reliability as a function of the interconnection resistances. In the case where the optimization is with respect to one failure, an alternate method may be used based on maximizing the quantity:

$$P_s W_s(r_c) + P_o W_o(r_c)$$

where P_s and P_o are as before, W_s and W_o are the relative powers for short and open failures respectively, and r_c is the interconnection resistance.

The computer is essential in the above analysis in all but the simplest cases, where no more than six diodes are involved. Programs have been written for generating and solving the loop equations corresponding to flat, cylindrical, and star-shaped matrix systems; for calculating the reliability of a system using either of the approximate schemes mentioned; and for maximizing the system reliability in some limited cases.

3. An Analysis of a Particular System

For purposes of elucidating the remarks in *Subsection 2*, the results from an analysis of a converter system employing two converters in series and three converters in parallel is presented in a series of graphs.

Figure 1 is a simplified drawing of the configuration being considered. E is the open-circuit voltage of the individual converters, R is the resistance of a single converter, and $r_c\,(=\alpha R)$ is the resistance of the interconnecting resistors. For convenience, r_c will be expressed as a factor α of R, the diode resistance. In all calculations, a matched load is used to maximize the power output.

In Fig. 2, the functional relationship between the maximizing factor α for the interconnection resistance and the probability of a failure being a short P_s is shown for the case in which the maximizing resistance is calculated assuming one failure and the case where it is calculated assuming two failures. It is seen that the two curves are very close together, and it was shown that a 0.1 variation in α produces a 0.001 change in the maximum relative power for either one or two failures. This implies that there is little difference in maximizing for one failure or two failures. Notice that for $P_s \leq 0.14$, $\alpha = 0$, which means physically that the interconnecting resistors would be completely shorted. Likewise, note that for $P_s \geqq 0.64$, α is infinite, meaning that the interconnecting resistors would be completely removed.

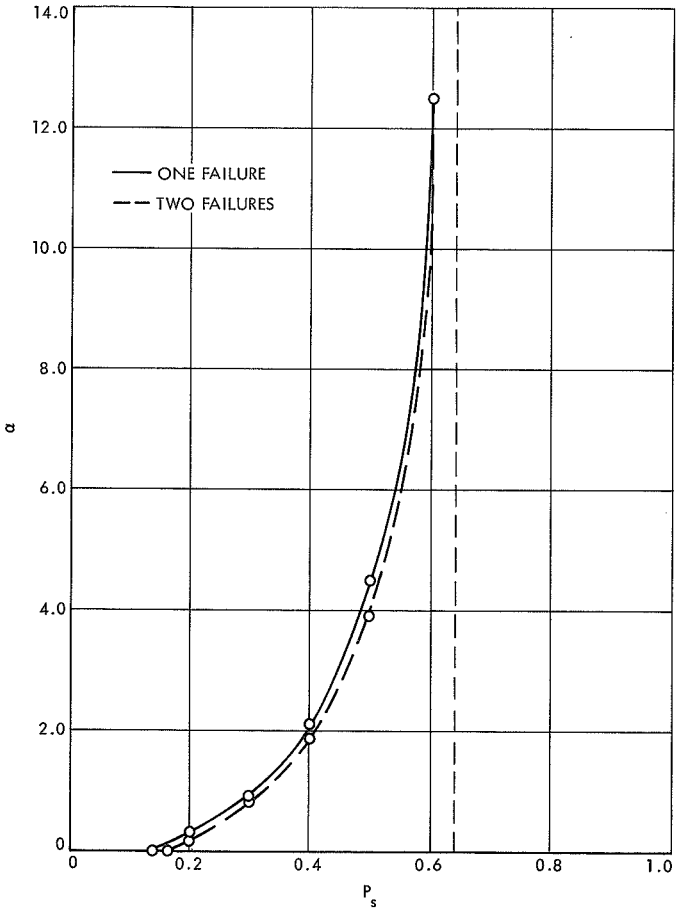

Fig. 2. Maximizing factor for interconnection resistance vs probability of shorted failures

Figure 3 shows how system reliability changes as a function of the relative power. This figure also shows how reliability changes with the type of failure that is most probable to occur. These curves are not smooth since there are only discrete power levels available. Also, the reliability for a system with either all open ($P_s = 0$) or all shorted ($P_s = 1.0$) failures is better than that for a system in which both types of failures can occur, since in the latter case the optimization value is a "compromise" between optimizing for just an open failure or just a shorted failure. The effect of having open failures in conjunction with a small number of shorted failures is quite detrimental for the configuration being studied, as Fig. 3 shows. Table 1 presents a more accurate picture of how the reliability varied with the relative power W and the probability of having shorted failures P_s.

4. System Application

The results of an optimization and reliability analysis, using the techniques presented in *Subsection* 2, are presented for a generator system having the following specifications:

Terminal voltage, V	3.0
Nominal power, W	150
Contingency factor, %	20
DC–DC conditioner efficiency, %	80
Converter reliability, %	95
Probability of short, %	60
Probability of open, %	40

The components, other than the converters, are assumed to have reliabilities of 100%. One more constraint is that the reliability is maximized in the peak power range, meaning that the system will be optimized for one failure.

A network of five converters in series and three in parallel is selected to be the configuration capable of meeting the above specifications. The diodes in this system must deliver 0.6 V at 25.00 A per converter, producing a gross power output of 225.0 W for this 15-converter system.

The curves for the maximizing factor α versus the relative power output for one failure occurring in the first, second, and third levels of the five-level configuration are shown in Fig. 4. By weighting the curves obtained for

Table 1. System reliability[a] for values of P_s and W

P_s	W								
	0.0	0.333	0.444	0.5	0.6	0.667	0.7	0.75	0.8
0.0	1.0	0.99975	0.99924	0.99732	—	0.98508	—	—	0.96672
0.25	1.0	0.99797	0.99184	0.97807	0.91993	0.91239	—	0.777/0.90896	—
0.50	1.0	0.99700	0.4479/0.99257	0.97730	—	0.97116	0.714/0.96658	—	—
0.75	1.0	0.99509	0.99305	0.98364	0.98328	0.96954	—	0.90883	—
1.00	1.0	—	—	0.99251	0.99165	—	—	0.97717	—

[a]The reliability at a relative power of 1.0 is 0.73509 in all cases.

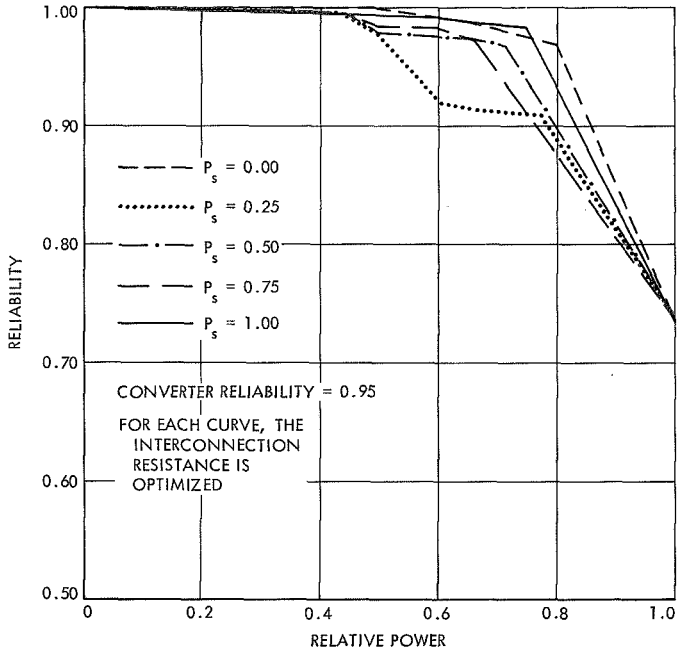

Fig. 3. System reliability vs relative power

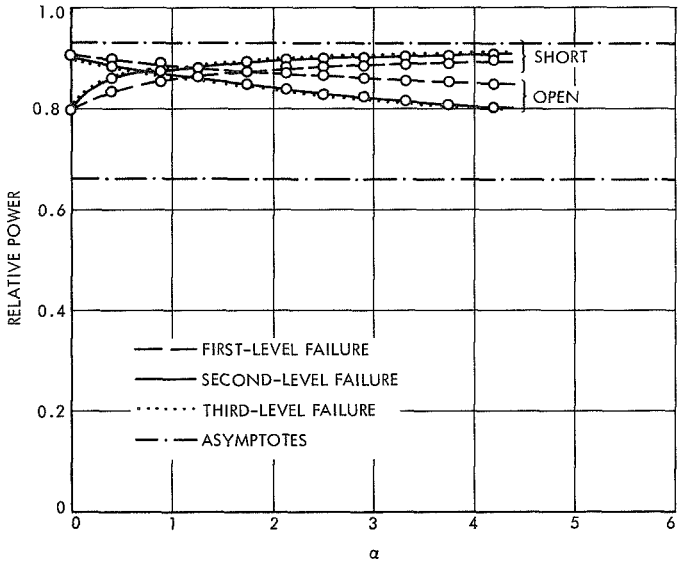

Fig. 4. Maximizing factor for interconnection resistance vs relative power

each level (as described in *Subsection* 2), three values for the maximizing factor were obtained, one for each level. These values were then weighted according to the probability of a failure occurring in the corresponding level. The result was an optimization factor of 1.90. This factor was then used in conjunction with a diode resistance of 0.024 Ω (= 0.6/25.00) to obtain a reliability curve. A sampling scheme (as described in *Subsection* 2) was used in calculating the reliability data which appears in Fig. 5. As this figure shows, the reliability at the required nominal power is approximately 0.985.

In summary, it has been shown that a 225-W system is necessary to achieve a nominal power output of 150 W, given a 20% contingency factor and 80% DC–DC conditioner efficiency. The generator system used to produce such a power output employed 15 converters in a 5-series, 3-parallel cylindrical configuration. Assuming a converter reliability of 0.95 and a shorted failure probability of 0.6, it was shown that the system reliability at the nominal power output (150 W) is 0.985.

5. Conclusions

There are some general conclusions that can be drawn concerning reliability and optimization as functions of system configuration and open–short failure probabilities. Figure 2 described the relationship between the maximizing factor α and the shorted failure probability P_s for a 2-series, 3-parallel system. The general shape of the curve (α monotonically increasing with P_s) will hold for all system configurations, but the points at which α goes to zero and infinity will shift. For systems in which there are a large number of series connections, the curve will shift to the right, while for systems in which there are a large number of parallel connections, the curve will shift to the left. At $P_s = 0$ and 1.0, $\alpha = 0$ and ∞, respectively; this is true regardless of the matrix dimensions.

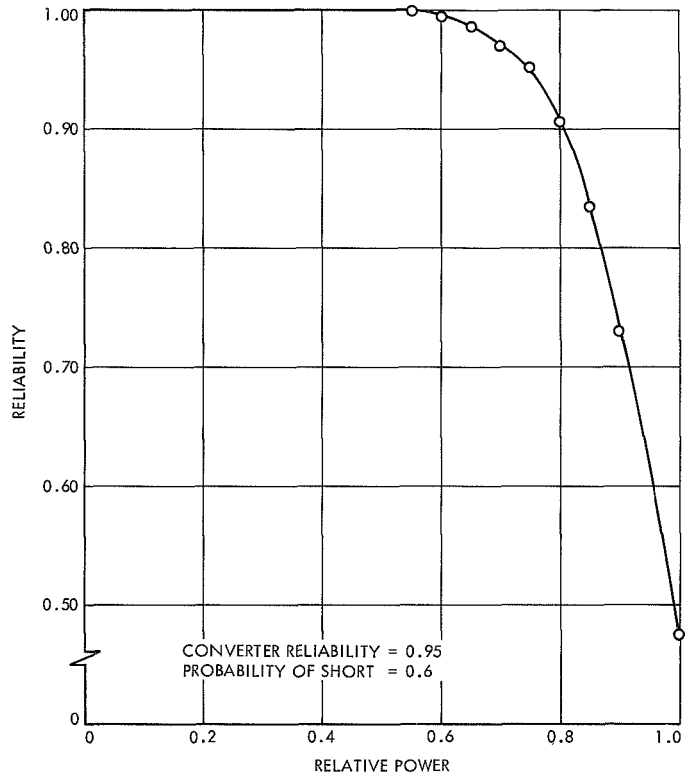

Fig. 5. System reliability vs relative power (sampling scheme)

In general, the most reliable systems have diode configurations that are dependent upon the probabilities of open and shorted failures. Thus, if there is a high probability of having open failures, the system should be designed to have a large number of parallel branches and vice versa for a high shorted failure probability. It was also noted that the effect of opens in a system optimized for this type of failure is identical to the effect of shorts in a system optimized for shorted failures, if the number of diodes in parallel equals the number in series.

Of the two methods presented for calculating reliabilities, the Monte Carlo method offers the greater generality and flexibility. This method was successfully applied in optimizing the design of a 150-W thermionic generator system. For generators requiring a large number of converters, however, the computation time quickly increases, requiring the development of new computational schemes.

All the calculation schemes presented here are based upon a linearized model for thermionic converters which, in reality, are not linear devices. Modification of the existing method to include nonlinear systems is being considered. Also, experimental work on a nonlinear system will be performed to estimate the accuracy of the reliability calculations for a linear system.

References

1. Shimada, K., deWinter, F., *Optimization of Thermionic Generator Systems of High Reliability,* presented at the Fifth Space Congress, Cocoa Beach, Florida, Mar. 11–14, 1968.

2. Holland, J. N., Bosseau, D. L., *Thermionic Converter Network Reliability,* General Atomic (John Jay Hopkins Laboratory) Report 6A-6102. Bureau of Ships, Department of the Navy, San Diego, Calif., Mar. 19, 1965.

B. A Proposed Laser Obstacle Detection Sensor for a Mars Rover, *W. L. Kuriger*[1]

1. Introduction

The exploration of Mars is expected to require the use of an unmanned surface roving vehicle. Because of the large and variable time delay involved in earth–Mars communications, such a vehicle would be required to traverse the Martian surface with minimal external control; specifically, the vehicle should be able to detect obstacles and avoid them by making small deviations from an otherwise pre-planned trajectory. It is the purpose of this article to analyze the requirements for an obstacle detection system and propose a specific configuration for such a sensor.

The surface of Mars has not yet been observed with anywhere near the resolution necessary to distinguish objects on the scale of meters; thus, possible distributions of obstacles are speculative. The highest resolution pictures of the Martian surface presently available (Refs. 1, 2,

[1]University of Oklahoma (NASA summer faculty fellowship program).

and 3) are those taken by *Mariners VI* and *VII*, and show features down to about 300 m in extent. The Martian terrain can be classified conveniently into four general types: heavily cratered terrain, featureless terrain, chaotic terrain, and polar ice caps. The heavily cratered terrain covers the largest portion of the Martian surface, and is, in many respects, similar to but somewhat smoother than the surface of the moon. The featureless terrain, of which the largest known example is the "desert" Hellas, consists of regions which appear absolutely smooth in photographs capable of resolving detail down to about 300 m. The chaotic terrain consists of jumbled short ridges and valleys, and is nearly devoid of craters. This type of surface was first discovered in the *Mariner VI* and *VII* photographs; its extent, causes, etc., are not yet known. The polar ice caps appear to be heavily cratered terrain with added drifts of "snow," probably frozen carbon dioxide. An extensive amount of work has been done with regard to probable obstacle distributions (Refs. 1 and 4), but this data is undergoing continuous revision as the *Mariner VI* and *VII* photographs are analyzed, and will undoubtedly be considerably revised when the much more complete and higher resolution data from *Mariner* Mars 1971 becomes available. By the time an exploratory vehicle is landed on Mars, the surface will be continuously mapped to a resolution of a few kilometers, and selected small areas will be photographed with a resolution of perhaps 50 m. At present, it appears that, with the possible exception of the chaotic terrain, the Martian surface will be sufficiently smooth that a roving vehicle will only occasionally encounter an obstacle.

The Martian atmosphere is some two orders of magnitude less dense than that of earth, with a mean surface pressure of about 7 mbar, and is considered to consist of about 80% CO_2 (by mass) with the remainder being largely inert gas, most likely nitrogen (Ref. 5). The Martian atmosphere is probably too tenuous to be a factor in the obstacle sensor design.

Moore (Ref. 6) has performed a preliminary analysis of requirements for a Martian surface navigation capability. He envisions a vehicle equipped with both a short-range obstacle detector, to serve a purely protective function, and a relatively long-range obstacle detector which would permit the vehicle to sense obstacles such as boulders, small craters, and steep slopes in time to change its heading and so avoid them. We consider only the second function.

Present plans are that the exploratory vehicle will be of six-wheeled articulated construction and will traverse the Martian surface at a typical rate of ½ km/h, with a maximum speed of perhaps 1½ km/h. The obstacle detection sensor should mount directly on the vehicle and be capable of detecting obstacles with dimensions as small as 0.5 m. Design contraints include that the sensor should be capable of operating in bright sunlight and, if possible, the sensor should weigh no more than 10 lb, contain no moving parts, and consume at most 10 W of power.

Since the identification of obstacles is greatly facilitated if range information is known, the only form of obstacle detector considered is a rangefinder, specifically one using electromagnetic radiation in the infrared–optical region to meet the resolution requirements and to best utilize the transmission medium and available technology. Optical rangefinders may be active or passive, that is, they may direct a beam of energy to the target or use a natural source such as sunlight, and they may utilize a number of different principles, which include time-delay measurements, triangulation, interferometry, and optical effects such as focussing and parallax in various guises. Several of these approaches are discussed in a report by Biernson, Euling, and Jarnagin (Ref. 7). The weight, power, and sunlight constraints imposed strongly favor an active rangefinder utilizing a laser, with a semiconductor injection laser being a particularly attractive choice because of its small size and weight and its compatibility with miniaturized electronics. The strictures on moving parts, coupled with the necessity to scan a significant area, militate against the use of triangulation or focussing techniques; thus, the sensor configuration which appears to be best adapted to the requirements of the Mars rover application is one utilizing an injection laser in the pulse time-delay measurement or radar mode. With the choice of rangefinder type made, the obstacle detector design divides into three major components: choice of scan configuration and design of the scan mechanism, the rangefinder design, and the devising of methods for interpreting the information obtained by the rangefinder.

2. Scan Requirements and Mechanisms

An upper bound to the range at which the rangefinder should operate is determined by the geometry of the situation. If we assume the sensor is located at a height of 2 m above the surface of the terrain, then, at ranges much greater than about 20 m, even gentle surface undulations would serve to mask pits and depressions entirely and would make it difficult to unambiguously discern the presence of a positive obstacle such as a boulder. Let us assume that it is desirable to scan an area extending from a few meters distant out to 20 or 30 m. This requires only

a small scan angle if the vehicle attitude and terrain surface are level, as is shown graphically in Fig. 1, but a considerable increase in scan angle is necessary to compensate for more realistic angles between vehicle attitude and the mean surface in front of the vehicle.

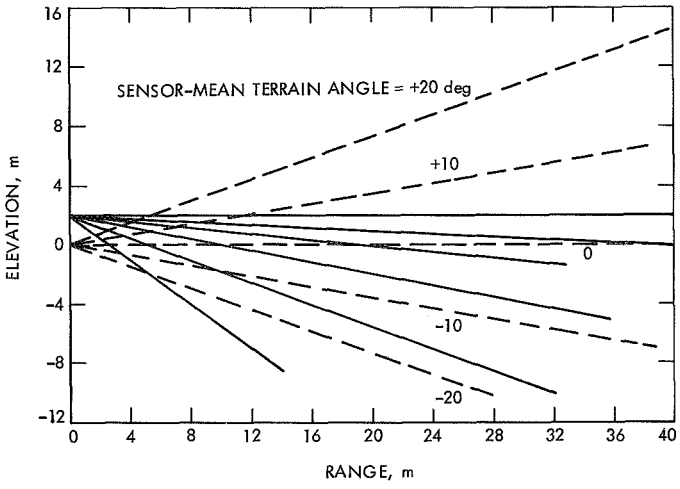

Fig. 1. Effect of angle between sensor and surface on range for fixed intervals of vertical scan (sensor height assumed to be 2 m)

A reasonable azimuthal scan requirement is that the observed area be at least as wide as the swath of the roving vehicle at useful elevation scan positions. A wider azimuthal scan would be desirable if large numbers of obstacles were expected, but since this is not the case, alternate vehicle headings can be explored simply by steering the vehicle.

Achieving the desired scan without the luxury of moving parts poses a difficult problem indeed. A large variety of electro-acoustic, electro-optic, and piezoelectric beam deflection techniques exist (Refs. 8 and 9), but none are capable of achieving large scan angles without considerable complexity and perhaps are not at all capable of this with the multimode output characteristic of an injection laser. Additionally, these techniques are best adapted to beams of very small diameter, while both transmitted and received beam diameters must be on the order of tens of millimeters in this application. If the expression no "moving" parts is interpreted to mean no wearing parts, a suitable elevation scan can be achieved by use of a resonant vibrating mirror of the fork or taut band type developed by the American Time Products Division of the Bulova Watch Company, and the much less stringent azimuth requirement can be met by use of a transmitting array. The specific scheme proposed employs an array of five laser diodes (operated one at a time) properly positioned along the focal plane of a convergent lens to give the azimuth pattern shown in Fig. 2, while the receiver beam is shaped into a fan pattern by use of a cylindrical lens and is not scanned in azimuth. Only one of the lasers in the array is operated during each elevation scan, so five elevation scans are required to completely scan the pattern. As Fig. 2 shows, the use of only five laser diodes at the particular spacing chosen is marginal in that the azimuthal beamwidth does equal the vehicle width (assumed to be 2 m) at ranges greater than 7 m, but the azimuthal resolution is better than 0.5 m only for ranges less than about 7 m. This situation is considerably alleviated by the fact that a particular portion of a scene will be scanned many times from slightly different aspects as the vehicle progresses.

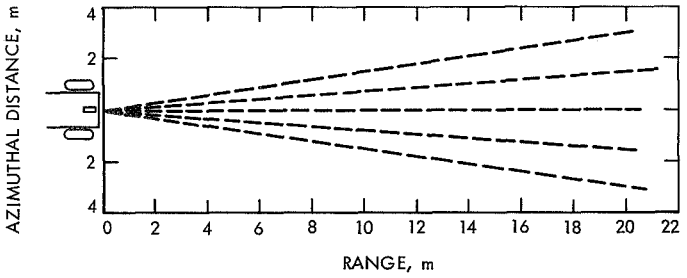

Fig. 2. Azimuthal beam paths for array of 5 laser diodes (diodes assumed spaced at 6-mm intervals in focal plane of lens with 80-mm focal length)

A specification for a vibrating mirror which should be within or at the state of the art includes a 25-Hz vibration frequency, ±12.5-deg peak mirror excursion (50-deg total beam deflection), and a 30- × 60-mm mirror size, with the long axis parallel to the axis of rotation. This size mirror permits the transmitter and receiver beams to be side by side; it might also be possible to use two separate vibrating mirrors if they can be synchronized sufficiently closely. The elevation scan is sinusoidal, but can be partially linearized by utilizing only a portion of the mirror excursion. If the mirror attitude is set so that its equilibrium position is looking down from the horizontal by 0.15 rad (8.6 deg) and its usable scan angle is ±0.25 rad (±14 deg), then it will scan a range from 5 m out to infinity when the vehicle attitude and surface are level, from 3 m out to about 13 m when the vehicle–mean surface angle is −0.25 rad, and from 13 m out to infinity when the vehicle–mean surface angle is +0.25 rad. Since the vehicle–mean surface angle should be this large for only brief periods, this range of scan angle appears to be adequate.

The beam swept out by the vertical scan moves at an angular rate of 68.5 rad/s in the vicinity of the mirror equilibrium point, so a transmitter pulse repetition rate of 10 kHz means that the terrain is sampled at 0.61-m intervals at the midrange distance of 13.3 m for the level vehicle attitude–level terrain case. The geometry of the situation automatically results in finer resolution being attained at closer ranges—the samples are spaced at approximately 6 cm at a range of 4 m—and less fine resolution at greater ranges, an eminently sensible arrangement. Since only one laser diode is operated on each vertical scan, the entire field is scanned once each 0.2 s, a time which is sufficiently short that vehicle pitching and rolling should only occasionally interfere with a scan. At the nominal condition of level vehicle attitude and level terrain, a vehicle traveling at a velocity of 0.139 m/s (0.5 km/h) will detect a given obstacle 900 times in the 5- to 30-m search range. This redundancy will be somewhat reduced by vehicle pitching, but is still of such a magnitude as to suggest spending some of it in combatting false alarms, that is, requiring that an obstacle be sensed several times in succession before the sensor signals the presence of an obstacle.

3. Rangefinder Design

The next topic considered is the design of the rangefinder used in the sensor. Major components of the sensor are shown in block diagram form in Fig. 3. The transmitter portion of the rangefinder consists of an array of five RCA TA7610 gallium–arsenide laser diodes, each equipped with its own driving circuitry. This laser diode has a typical output of 13 W, and the emitting area is on the order of 3×225 μm. The diffraction-limited beamspread for the smaller laser dimension is on the order of 0.3 rad, and since the target area should be illuminated with a beam of the smallest possible diameter to minimize target-induced pulse spreading and split returns, a collimating lens is necessary. It is difficult to predict precisely the effect of a spherical lens on the laser beam since it is multimode and not circularly symmetric, but a 25-mm $f/3.2$ simple lens should collect at least 80% of the radiation emitted by any one of the five diodes and should project it onto a spot never larger than 0.1 m in diameter for ranges up to 30 m. The diodes must be spaced at 6-mm intervals along the lens focal plane to achieve the scan coverage of Fig. 2, and individual adjustments of diode orientation will probably be necessary to achieve the desired results. The function of the pulser/timer is to sequentially operate one laser of the array on each elevation sweep and to fire the laser diodes at a 10-kHz rate and with a pulse duration of about 4 ns.

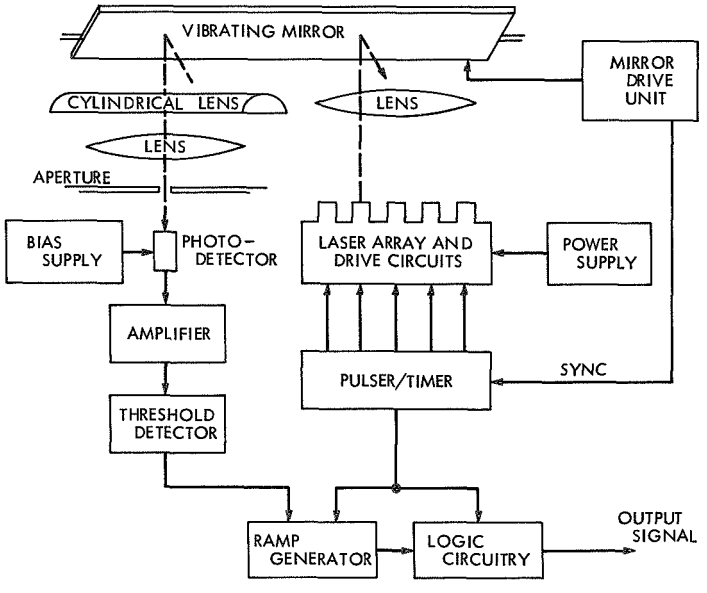

Fig. 3. Obstacle-detecting sensor

The receiver portion of the rangefinder consists of collecting optics, a photodetector, an amplifier, and a threshold detector. The receiver optics consists of a cylindrical lens followed by a 25-mm-diameter simple lens to produce a receiver beamwidth of 3 mrad in elevation and 0.4 rad in azimuth. This particular beamshape includes in its field of view all the azimuthal area which can be illuminated by the transmitter, but is otherwise as small as possible to reduce the amount of background solar radiation intercepted. The receiver optical system also contains a 50-Å optical filter to further discriminate against background radiation. The optical bandwidth is made as narrow as laser characteristics permit. Room temperature gallium–arsenide injection lasers emit at a nominal wavelength of 9020 Å, with an output wavelength-spread on the order of angstroms caused by multimoding and by heating within the duration of a pulse. There are differences between diodes on the order of tens of angstroms because of material and processing variations, and the output wavelength shifts with diode temperature at a rate of approximately 1.75 Å/°C; thus, a 50-Å optical bandwidth is a compromise between obtaining good background rejection and requiring tight wavelength control.

Sensor performance is calculated for three different types of detectors—silicon PIN photodiode, avalanche photodiode, and photomultiplier tube—for the case that detection is based on a threshold criterion. Parameter

Table 1. Parameter symbols and values used in the calculation of Mars roving vehicle rangefinder performance

Symbol	Parameter	Value
A_r	Receiver antenna area	0.49×10^{-3} m^2
A_v	Voltage gain of postdetection amplifier	–
B	Optical bandwidth	50 Å
c	Velocity of light	3×10^8 m/s
e	Electronic charge	1.602×10^{-19} C
Δf	Postdetection bandwidth	250 MHz
F	Noise factor of postdetection amplifier	2
G	Internal gain of photodetector	1 for PIN diode; 5×10^4 for photomultiplier; 20, 100, or 200 for avalanche photodiode
h	Planck's constant	6.625×10^{-34} J-s
I_{av}	Mean value of photocathode current	–
I_d	Photodetector dark current (at photocathode)	0.15 nA for PIN diode; 3.25×10^{-16} A for photomultiplier; $10^{-8}/G + 0.5 \times 10^{-12}$ A for avalanche photodiode
k	Boltzmann's constant	1.38×10^{-23} J/°K
L	Ground range	–
m	Exponent of internal gain for noise power	2 for photomultiplier; 2.3 for avalanche photodiode
M	Solar spectral irradiance at 0.9 μm	0.04 W/m^2-Å
P_b	Background power incident on detector photocathode	–
P_r	Signal power incident on detector	–
P_t	Laser power output (peak)	13 W
Q, Q_s, Q_n	Quantum efficiency, photoelectrons/photon	0.5 for PIN diode; 3×10^{-3} for photomultiplier; $Q_s = 0.3$, $Q_n = 0.9$ for avalanche photodiode
R	Range	–
R_L	Photodetector load resistance	50 Ω
T	Absolute temperature	290°K
T_a	Martian atmospheric transmission at 0.9 μm	1
V_{sig}	Signal voltage at output of postdetection amplifier	–
V_n	Noise voltage at output of postdetection amplifier	–
α_r	Receiver antenna azimuthal beamwidth	0.4 rad

Table 1 (contd)

Symbol	Parameter	Value
α_v	Receiver antenna vertical beamwidth	3 mrad
Γ_r	Efficiency of receiver optics	0.5
Γ_t	Efficiency of transmitter optics	0.8
ξ	Martian surface reflectivity at 0.9 μm	0.3
Φ	Angle between direction of sun and surface normal	—
λ	Operating wavelength	0.902 μm

symbols and values used in the calculations are given in Table 1. The choice of postdetection bandwidth is dictated by the requirement of maintaining a sufficiently fast risetime to preserve the pulse leading edge, and the bandwidth requirement in turn places an upper bound on the allowable load resistance. The value of solar spectral irradiance is determined from quantities given in Allen (Ref. 10), while the value for Martian surface reflectivity is from Meisenholder (Ref. 11). The receiver antenna area is selected to be small but comparable to the area required for the transmitter optics, and all other parameter values are dictated by characteristics of available components. The detector specifications are based on a Hewlett-Packard HP 4207 PIN photodiode, a Texas Instruments TIXL55 avalanche photodiode, and an RCA C70102B photomultiplier tube.

Using the symbols and values given in Table 1, the signal power delivered to the detector's photocathode is

$$P_r = \frac{P_t \Gamma_t \Gamma_r \xi T_a A_r}{2\pi R^2} = \frac{0.1219 \times 10^{-3}}{R^2} \tag{1}$$

which is 0.135 μW at a range of 30 m and 4.87 μW at a range of 5 m.

The solar background power at the detector photocathode is given by

$$P_b = \frac{M \alpha_v \alpha_r T_a B \xi \Gamma_r A_r \cos \Phi}{2\pi} \tag{2}$$

and taking the worst-case situation of the sun directly overhead, so $\Phi = 0$, P_b is found to be 0.028 μW and is independent of range.

If the photodetector is characterized by a quantum efficiency Q—we must use "fast" and "slow" values Q_s and Q_n for the case of an avalanche photodiode—and a dark current I_d, the mean value of current leaving the photocathode is

$$I_{av} = I_d + \frac{e\lambda (Q_s P_r + Q_n P_b)}{hc} \tag{3}$$

and the standard deviation is given by $(2e\Delta f I_{av})^{1/2}$. The distribution of photoelectrons is Poisson, but since there are many electrons per independent observation interval, the process is adequately modeled by gaussian statistics. In the latter form, the shot noise due to incident signal and background radiation and internal effects may be conveniently combined with the thermal noise of the detector load resistance and the noise contributed by a postdetection amplifier. If the photodetector has internal gain G and is loaded by a preamplifier with input impedance R_L, noise factor F, and voltage gain A_v, and if the preamplifier passband is set to pass the high frequencies associated with a fast pulse risetime but not the low frequency fluctuations induced by scanning terrain of varying albedo, etc., the rms noise voltage output of the preamplifier is

$$V_n = A_v (G^m R_L^2 2e\Delta f I_{av} + F 4kT\Delta f R_L)^{1/2} \tag{4}$$

The mean value of preamplifier output voltage during a signal pulse is given by

$$V_{sig} = \frac{A_v R_L G Q_s e \lambda P_r}{hc} \tag{5}$$

and the voltage signal-to-noise ratio is obtained by combining the various equations:

$$\frac{V_{sig}}{V_n} = \frac{\left(\frac{e\lambda}{hc}\right) R_L G Q_s P_r}{\left\{2e\Delta f G^m R_L^2 \left[I_d + \frac{e\lambda}{hc}(Q_s P_r + Q_n P_b)\right] 4kT\Delta f R_1 F\right\}^{1/2}} \tag{6}$$

Table 2. Voltage signal-to-noise ratios at the postdetection amplifier output for various types of detectors

Detector	$\frac{V_{sig}\ (20\text{-m range})}{V_n\ (\text{signal off})}$	$\frac{V_{sig}\ (20\text{-m range})}{V_n\ (\text{signal on})}$	$\frac{V_{sig}\ (30\text{-m range})}{V_n\ (\text{signal off})}$	$\frac{V_{sig}\ (30\text{-m range})}{V_n\ (\text{signal on})}$
PIN photodiode	0.276	0.276	0.123	0.123
Photomultiplier	9.41	2.75	4.18	1.88
Avalanche photodiode				
G = 20	3.29	3.24	1.46	1.45
G = 100	13.25	9.76	5.89	5.02
G = 200	17.05	10.34	7.58	5.71

Numerical values are summarized in Table 2 for ranges of 20 and 30 m for the worst-case situation of the sun directly overhead.

The dominant source of noise in the case of the PIN photodiode detector is thermal noise in the load resistance, and the V_{sig}/V_n results (Table 2) indicate that an increase of transmitted power or receive antenna area of 2 orders of magnitude would be necessary in order to use this particular device (a signal-to-noise ratio of 10 is the approximate requirement). The photomultiplier's high internal gain makes load thermal noise negligible, but its low quantum efficiency and the relatively large value of background illumination limit its performance. The avalanche photodiode is a semiconductor with properties that fall inbetween a silicon photodiode and a photomultiplier, but it has two peculiarities which degrade its signal-to-noise performance somewhat. One is that all incident photons are not immediately absorbed, and as a result the device has a substantially lower value of ac quantum efficiency than dc quantum efficiency. The other undesirable characteristic is that the avalanche internal gain mechanism is not noiseless; this is accounted for in the device model by the exponent of the gain being different for noise power than for signal power. This latter characteristic causes an optimum value of gain which maximizes the signal-to-noise ratio for any particular set of circumstances; the optimum value of gain for the particular set of parameter values used in the calculations is beyond the "typical" attainable value of 200 but does not result in performance significantly better than that achieved with a gain of 200. The results given in Table 2 indicate that an avalanche photodiode operated at a gain on the order of 100 or 200 yields an adequate signal-to-noise ratio at a range of 20 m and a marginal one at 30 m; thus, this is the device that would be incorporated into the sensor.

For the case that signal detection is based on a threshold criterion, the signal-to-noise ratio necessary in a particular application is determined by the need to set a threshold voltage level which is sufficiently high that it is only rarely exceeded by noise peaks in the absence of a pulse but not so high that it fails to detect signal pulses. To calculate the threshold level necessary to ensure that false alarms occur no more than, say, once a month, we observe that there are on the order of 60 signal pulses/line scan, 300 pulses/field, 1,500 pulses/s, and 2×10^9 pulses/mo (assuming 12 h of operation per day). From sampling theory, independent voltage samples occur every 2 ns for a 250-MHz bandwidth, and if range gating is employed (this would occur automatically if the ramp scheme to analog-process the range data is used) only to consider times for a pulse to return from up to a 30-m range (200 ns), there are 100 independent observation intervals/pulse, and on the average half of these would occur before receipt of a signal pulse. Thus, a false alarm rate of 1 pulse/mo requires that the probability of the signal-absent noise exceeding the threshold be about 10^{-11}, but this number is not particularly critical because of the rapid exponential decline of the wings of gaussian functions. If we define a missed pulse as one which is not detected in one observation interval of 2 ns, then the probability of a missed pulse is equal to the probability that the signal-present noise exceeds the difference between the mean signal level and the threshold voltage. Since the sensor might detect a given obstacle as many as 900 times as the vehicle progresses, and since this calculation will result in a threshold which will be increasingly exceeded by the signal level as the range to the obstacle is reduced, a reasonable requirement is that a missed pulse should occur no oftener than once a minute, which in turn requires that the probability of the signal-present noise exceeding the mean signal–threshold differences be about 10^{-5}. From tables of gaussian probabilities, we can write

$$\left.\begin{aligned} V_T &\geqq 6.71\, V_n\ (\text{signal off}) \\ V_{sig} - V_T &\geqq 4.26\, V_n\ (\text{signal on}) \end{aligned}\right\} \qquad (7)$$

where V_T signifies the threshold voltage. Combining these equations yields an equation that constrains possible values of signal-to-noise ratios.

$$\frac{6.71}{\frac{V_{sig}}{V_n\,(\text{signal off})}}+\frac{4.26}{\frac{V_{sig}}{V_n\,(\text{signal on})}}\leq 1 \qquad (8)$$

A similar analysis shows that the signal-to-noise requirements can be relaxed if it is required to sense the presence of an obstacle a number of times before triggering an output. If it is required to detect an obstacle on four successive frames, the equation that constrains possible values of signal-to-noise ratios becomes

$$\frac{2.91}{\frac{V_{sig}}{V_n\,(\text{signal off})}}+\frac{4.55}{\frac{V_{sig}}{V_n\,(\text{signal on})}}\leq 1 \qquad (9)$$

Equations (8) and (9) are plotted in Fig. 4. Note that the requirement of a multiple indication of an obstacle not only eases the performance requirements but also greatly reduces the probability of false alarms caused by anomalies not considered in this analysis.

The ranging accuracy of the proposed rangefinder is difficult to calculate, but can be estimated from experimental results on other systems. A laser profilometer reported by Hopson (Ref. 12) uses the same type of threshold detection system considered here with about the same overall pulse risetime, and experimental results for that system indicate a range accuracy of ±10 cm.

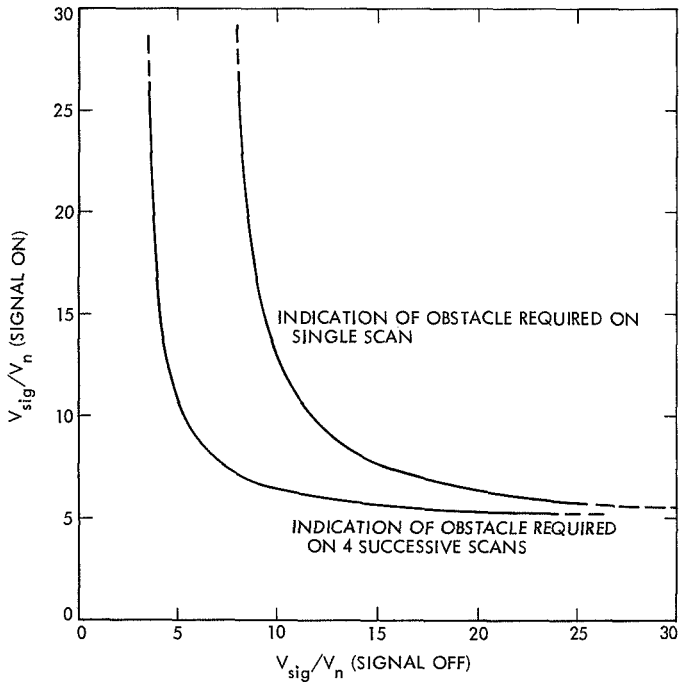

Fig. 4. Curves relating minimum required signal-to-noise ratios for proper sensor operation

4. Interpretation of Rangefinder Returns

The interpretation of returned signals to determine whether or not an obstacle is present can be accomplished in a variety of ways. One possible method is to use a fast timer to measure the elapsed time between the emission of a pulse and the detection of the return. This information is then fed to the vehicle computer along with vehicle attitude information. The angular coordinates of each pulse are known from timing considerations, so the computer can be programmed to distinguish obstacles to any desired degree consistent with the sensor resolution. Another possible method, which might not require the use of the vehicle computer at all, is to convert each elevation scan into an analog waveform containing the desired information. If a fast ramp is initiated when a pulse is transmitted and terminated upon receipt of a return signal or the passage of 200 ns (the time for a signal to travel 30 m and return), whichever comes first, the range information will be preserved as a sequence of equally spaced pulses whose amplitudes are proportional to range. In the case of level terrain, the pulse train for each individual sweep would increase approximately quadratically in amplitude with time on a scale determined by the angle between vehicle and terrain. The presence of a positive obstacle, such as a boulder, would be manifested by a smaller than normal or even negative increase in amplitude between successive pulses, while a larger than expected increase would signal the presence of a negative obstacle, such as a fresh crater. The technique of comparing each pulse's amplitude with that of its immediate predecessor ignores nearly all the information in the return but looks specifically for the most characteristic indication of an obstacle—the presence of a discontinuity in range as a line-of-sight is swept. Unfortunately, it does not appear feasible to detect obstacles on the basis of pulse-to-pulse differences only. As shown in Fig. 5, the angle between vehicle and mean terrain is a significant factor. The apparent asymmetry between the three curves of Fig. 5 is caused by the nonlinearity of the sinusoidal scan compensating the geometric range nonlinearity in one case and complementing it in the other. Range differences between successive pulses vary considerably, as summarized in Table 3.

An adequate test can be mechanized using the range at each point within an elevation sweep. Dividing the

Table 3. Range differences between successive pulses at several ranges and vehicle–mean terrain angles for the proposed sensor operating on flat terrain

Nominal ground range, m	ΔR, m		
	Vehicle–mean terrain angle = −10 deg	Vehicle–mean terrain angle = 0 deg	Vehicle–mean terrain angle = +10 deg
5	0.090	0.077	0.035
10	0.327	0.359	0.289
20	1.178	1.394	1.300
30	2.558	3.192	2.964

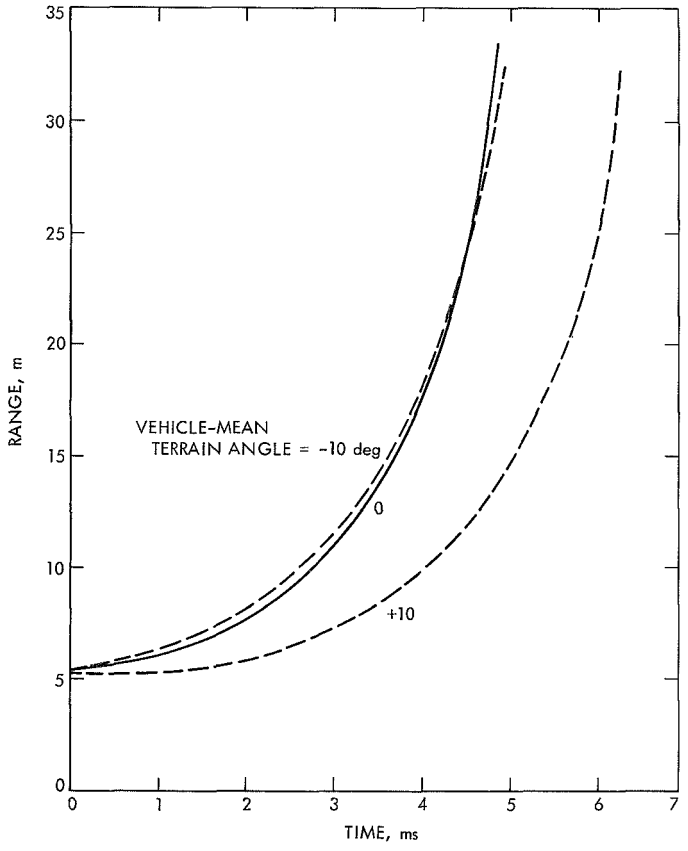

Fig. 5. Envelopes of range vs time for 3 different vehicle–mean terrain angles (range is distance from 2-m high sensor to flat surface; time is measured from instant that 5-m ground range (5.385-m slant range) is achieved)

range difference between successive pulses by the range squared ($\Delta R/R^2$) results in a number which is approximately constant for flat terrain, and can thus form the basis for generating a detection criterion. For proper interpretation of the rangefinder returns, it is necessary that the angle between the vehicle and mean terrain be within ±10 deg for each sweep. It is assumed that a 0.5-m step is an obstacle, while a 0.2-m step is not.

Because of the geometry, positive (step up) and negative (step down) obstacles may best be discerned by different criteria. A distinctive feature of a positive obstacle is that the range increase is small or zero for several successive pulses, as the scan travels from the bottom of the obstacle to the top. Thus, one method for determining the presence of a positive obstacle is to count the number of pulses for which $\Delta R/R^2$ falls below a fixed threshold. The return of greater than some predetermined number of successive pulses (e.g., 3 or 4) for which $\Delta R/R^2$ was below threshold would signal an obstacle. As an indication of the sensitivity of this criterion, the number of successive pulses necessary for the sensor to "see" the top of positive 0.2- and 0.5-m step obstacles is given in Table 4. The figures indicate that this particular criterion fails at the 5-m range, because it cannot distinguish a 0.2-m step from a 0.5-m step over the complete range of vehicle–mean terrain angles, but can be used at greater ranges. The data of Table 4 show that it would be desirable to make the number of pulses required to signal an obstacle dependent on the range.

Table 4. Pulses required for sensor to scan from bottom to top of 0.2- and 0.5-m positive step obstacles at various ranges and vehicle–mean terrain angles

Nominal ground range L, m	Vehicle–mean terrain angle, deg	Number of pulses	
		Positive 0.2-m step at range L	Positive 0.5-m step at range L
5	+10	15	37
	0	7	17
	−10	6	14
10	+10	4	9
	0	3	8
	−10	4	8
20	+10	2	4
	0	2	4
	−10	2	5
30	+10	1	3
	0	1	3
	−10	2	4

On the other hand, we suggest that the criterion for detection of a negative obstacle be the occurrence of a value of $\Delta R/R$ larger than a predetermined threshold. Table 5 gives values of the range difference between successive pulses divided by the range, $\Delta R/R$, and indicates that this criterion is adequate to detect negative obstacles if the threshold is set at approximately 0.180. The use of the quantity $\Delta R/R$ rather than $\Delta R/R^2$ yields a criterion that is more independent of range and terrain angle.

Table 5. Range differences between successive pulses divided by range for 0.2- and 0.5-m negative step obstacles for various ranges and vehicle–mean terrain angles

Nominal ground range L, m	Vehicle–mean terrain angle, deg	$\Delta R/R$		
		No obstacle	Negative 0.2-m step at range L	Negative 0.5-m step at range L
5	+10	0.006	0.097	0.205
	0	0.014	0.104	0.211
	−10	0.017	0.106	0.213
10	+10	0.028	0.117	0.223
	0	0.034	0.122	0.227
	−10	0.032	0.120	0.226
20	+10	0.063	0.148	0.250
	0	0.066	0.151	0.253
	−10	0.057	0.143	0.246
30	+10	0.095	0.177	0.276
	0	0.098	0.180	0.279
	−10	0.080	0.164	0.264

Thus, it appears entirely feasible to discern the presence of obstacles by relatively simple processing, but additional effort would be required to thoroughly evaluate this aspect of the problem.

5. Conclusions

The proposed sensor contains relatively small, light, and few optical components and the electronic components are all of the miniature solid-state type; thus, the weight of the overall sensor is primarily that of the mechanical packaging. It appears entirely feasible to hold the overall weight to 10 lb or less. If we assume a power efficiency of 0.1% for the laser diodes, a pulse duration of 4 ns, and a pulse repetition rate of 10 kHz half of the time (no transmission during vibrating-mirror scan retrace), the power required by the laser diodes is about 0.26 W. The vibrating-mirror drive power is on the order of 10 mW; thus, the power requirements are primarily those of the auxiliary electronics, and an overall power requirement of a few watts should be attainable. It appears feasible to discern whether or not the rangefinder returns indicate the presence of an obstacle by use of relatively simple signal-processing techniques, thus allowing the sensor to be a self-contained unit.

References

1. *Mariner-Mars 1969: A Preliminary Report,* NASA SP-225. National Aeronautics and Space Administration, Washington, D.C.
2. Leighton, R. B., *The Surface of Mars,* pp. 26–41. Scientific-American, New York, May 1970.
3. Leighton, R. B., et al, "Mariner 6 and 7 Television Pictures: Preliminary Analysis," *Science,* Vol. 166, pp. 49–67, Oct. 3, 1969.
4. *Mars Surface Models (1968),* NASA SP-8020. National Aeronautics and Space Administration, Washington, D.C., May 1969.
5. *Models of Mars Atmosphere (1967),* NASA SP-8010. National Aeronautics and Space Administration, Washington, D.C., May 1968.
6. Moore, J. W., *Surface Navigation on Mars,* paper presented at the National Space Meeting of the Institute of Navigation, Moffett Field, Calif., Feb. 17–19, 1970.
7. Biernson, G. A., Euling, R., and Jarnagin, W. S., *Range Sensor Techniques for Automatic Object Identification,* Final Report AFCRL Contract F 19628-69-C-0071. Air Force Cambridge Research Laboratory, Bedford, Mass., Nov. 1969.
8. Fowler, V. J., and Schlafer, J., "A Survey of Laser Beam Deflection Techniques," *Proc. IEEE,* Vol. 54, pp. 1437–1444, Oct. 1966.
9. W. Kulcke, et al, "Digital Light Deflectors," *Proc. IEEE,* Vol. 54, pp. 1419–1429, Oct. 1966.
10. Allen, C. W., *Astrophysical Quantities,* pp. 140 and 155. University of London Athlone Press, London, England, 1955.
11. Meisenholder, G. W., *Planet Illuminance,* Technical Report 32-361. Jet Propulsion Laboratory, Pasadena, Calif., 1962.
12. Hopson, J. E., *Low Altitude Laser Measurement System,* Technical Report AFFDL-TR-67-176. Air Force Flight Dynamics Laboratory, Wright-Patterson AFB, Ohio, Dec. 1967.

C. Automated Test Techniques for Guidance and Control Subsystems, *R. E. Williamson*

1. Introduction

The long-range objective of this effort is the development of guidance and control (G&C) support equipment technology to meet the requirements of future planetary missions. The specific near-term goals, which are directed toward the support of the thermoelectric outer planet spacecraft (TOPS) project, include the following: (1) development of test requirements for the TOPS G&C subsystems, (2) development of automated test techniques to implement the TOPS requirements, and (3) demonstration of the test techniques with a generalized support equipment approach centered around a small general-purpose computer.

2. Test Requirements for TOPS G&C Subsystems

One of the major tasks for this fiscal year is the development of a baseline test requirements document for the TOPS G&C subsystems (electrical power, attitude control, scan, and approach guidance). The objectives of this effort are twofold: (1) to assure that a testing capability is implemented in the subsystem designs, and (2) to identify the types of test functions which must be implemented in future support equipment designs.

The outer planet missions require advanced design approaches for the G&C subsystems which result in new elements to be tested and new complexities in testing requirements. Following are examples of some of the new designs planned for the G&C subsystems.

Approach guidance. This is a new subsystem required for navigation to the outer planets. Although the test technology will be similar to that required for the spacecraft science vidicon and imaging systems, there will be unique test requirements for the approach guidance subsystem.

Attitude control and scan. The attitude control subsystem is completely different from those previously employed due to increased accuracy and reliability requirements. Some of the new elements include: digital inertial and celestial sensors, digital attitude control electronics, hydrazine thrusters for coarse attitude propulsion, reaction wheels or pulsed plasma jets for fine attitude corrections, and multi-redundant circuits and components.

Electrical power. The radioisotope thermoelectric generators (RTGs) planned as the power source for the outer planets missions represent new elements in checkout. Associated with the RTGs is a new design for the power conditioning equipment. As with other spacecraft subsystems, considerable redundancy is required to achieve the long-life requirements.

Spacecraft computer interfaces. The G&C subsystems designs include a strong dependency upon the spacecraft computer. In addition to the normal functions of subsystem mode control, the computer is used to detect failures in the subsystems, confirm them, and take corrective action to reestablish a desired functional state whenever possible. Simulation of the computer is required when testing the subsystems at the subassembly and subsystem level.

3. Automated Test Techniques

A second major task for this fiscal year is the development of test techniques to implement the baseline test requirements. Automated techniques, using a computer-oriented test system approach, are being planned for most tests. Development of the techniques will include preparation of functional specifications for: (1) the software routines and algorithms required to perform the test functions, (2) the hardware required to interface the spacecraft subsystem and the computerized test set, and (3) any special-purpose hardware required with the test set, such as signal sources.

The reasons for the emphasis upon an automated test system are as follows:

Spacecraft complexity. A comparison of the complexity of the TOPS spacecraft with the *Mariner* Mars 1971 spacecraft shows a small increase in the number of actual parts. However, due to the use of large-scale integration on TOPS, the equivalent number of parts is greatly increased (estimated equivalent parts on TOPS = 900*k*, *Mariner* Mars 1971 = 100*k*). Associated with the parts increase are expansions of the spacecraft functions with the consequent escalation in testing requirements. One significant area of increased complexity is in the expansion of spacecraft modes associated with the implementation of multi-redundancy throughout the subsystems. The amount of data to be handled is such that automation is required to assure thorough system validation.

Technical requirements. Simulation of the spacecraft computer during subassembly and subsystem testing will require an automated test set which can operate synchronously with the spacecraft subsystem. Execution of test sequences which have time limitations also will call for automated testing. The increased use of digital components on the TOPS spacecraft provides an advantage for

the automated approach in that the digital circuits readily adapt to the interfaces of a computerized test system.

Test reliability. Reliability considerations for the long duration outer-planet missions will have a significant influence upon testing operations. Control of the test environment and of all pre-launch spacecraft operations will become more important than has been necessary for present spacecraft. With automated testing, the capability exists to provide greater control of testing and to make tests less subject to human errors. Test repeatability is an example where improved test control is possible with automated techniques. One of the weakest characteristics of manual testing, yet one of the strongest points of automated testing, is the ability to repetitively perform tests in precisely the same way. Identification of potential failures through trend analysis requires test repeatability.

4. Computer-Oriented Test System

A computer-oriented test system (CTS) will be used to develop and demonstrate the automated test techniques required to support the TOPS G&C subsystems. During this fiscal year, a functional specification will be prepared for the system design—including software and hardware—of the overall automated test set. Software development will be started using a leased computer, a Honeywell DDP-124, which is shared with the Astrionics Division.

Following is a discussion of past CTS technology development and future plans.

Past CTS technology development. The initial emphasis in developing a CTS technology was directed towards testing spacecraft computer subsystems. To demonstrate the basic capabilities of an automated test system, a prototype CTS was assembled and interfaced with a *Mariner* Mars 1969 central computer and sequencer (CC&S). The prototype system was used to develop and demonstrate the following:

(1) Capability for automatic control and verification of the performance of the test hardware in a real-time environment. The test system receives, time tags, decodes, and processes all test data and prints all changes and errors. Test command sequences are output at pre-determined times. In the automatic mode, the test data is compared with reference data generated by a software simulator which runs concurrently with the CC&S.

(2) Capability for operational flexibility and operator interaction. The necessary controls, displays, and software are provided such that the operator can apply stimuli and verify the hardware performance in a manual mode. New tests can be set up from operator instructions for entry into the test library.

In December 1969, CTS development for flight computer subsystems, including responsibility for the prototype CTS, was transferred to the Astrionics Division. The Guidance and Control Division retained responsibility for development of the CTS technology required to support G&C spacecraft subsystems. The technology base developed with the prototype CTS is being utilized in applying the automated testing approach to the more complex TOPS G&C subsystems.

Future CTS technology development plans. It is currently planned to assemble a CTS in fiscal year 1972 to demonstrate the automated test techniques required for the TOPS G&C subsystems with breadboards or simulations of the TOPS subsystems. In addition to developing the test techniques, consideration will be given to expanding the current CTS technology in the following areas:

(1) *Operational flexibility.* The same basic test system design is to be adaptable to testing all G&C subsystems, and adaptable to changes in the flight hardware and test procedures. The test system developed for the outer planet missions is to have the capability for reuse on follow-on missions.

(2) *Man–machine interaction.* Proper data presentation is required to permit human review and judgment. Operator control of the test sequences will be necessary with safeguards to prevent damage to the spacecraft. Hardcopy documentation of all test anomalies and all operator actions must be included.